Spectroscopy of an extreme [OIII] emitting active galactic nucleus at z = 3.212: implications for the reionisation era

Mengtao Tang[1]⋆, Daniel P. Stark[2], Richard S. Ellis[1], Stéphane Charlot[3], Anna Feltre[4],
Alice E. Shapley[5] and Ryan Endsley[2]

[1] *Department of Physics and Astronomy, University College London, Gower Street, London WC1E 6BT, UK*
[2] *Steward Observatory, University of Arizona, 933 N Cherry Ave, Tucson, AZ 85721, USA*
[3] *Sorbonne Université, CNRS, UMR7095, Institut d'Astrophysique de Paris, F-75014, Paris, France*
[4] *INAF - Osservatorio di Astrofisica e Scienza dello Spazio di Bologna, Via P. Gobetti 93/3, 40129 Bologna, Italy*
[5] *Department of Physics and Astronomy, University of California, Los Angeles, 430 Portola Plaza, Los Angeles, CA 90095, USA*

14 March 2022

ABSTRACT

Reionisation-era galaxies often display intense nebular emission lines, both in rest-frame optical ([O III]+Hβ) and ultraviolet (UV; C III], C IV). How such strong nebular emission is powered remains unclear, with both active galactic nuclei (AGN) and hot stars considered equally viable. The UV continuum slopes of these early systems tend to be very blue ($\beta < -2$), reflecting minimal dust obscuration, young ages, and low metallicities. This contrasts with narrow-lined AGN at $z \sim 2-3$, whose UV slopes are significantly redder ($\beta > -1$) than typical star-forming systems in the reionisation era. To investigate the properties of AGN in the reionisation era, we have conducted a search for potential examples of rare analogues with blue continua at intermediate redshift ($z \sim 2-3$). Our goals are to determine whether AGN with intense line emission and blue continua exist and thereby to establish the range of rest-frame UV and optical line ratios in this population. In this paper we report the detection of a X-ray luminous AGN at $z = 3.21$ (UDS-24561) with extreme [O III]+Hβ line emission (EW = 1300 Å) and a blue UV continuum slope ($\beta = -2.34$). MMT/Binospec and Keck/MOSFIRE spectra indicate rest-frame UV line ratios consistent with AGN photoionisation models and rest-frame optical lines with both a narrow component (FWHM = 154 km/s) and extended broad wings (FWHM = 977 km/s), consistent with outflowing gas. We describe how such objects can be identified in future *JWST* emission line surveys in the reionisation era, thereby providing a valuable census of AGN activity at $z > 6$ and understanding their contribution to cosmic reionisation.

Key words: cosmology: observations - galaxies: evolution - galaxies: formation - galaxies: high-redshift - galaxies: active

1 INTRODUCTION

Studying the reionisation of the intergalactic hydrogen is a major frontier in modern astrophysics, and provides important clues to understanding the history of cosmic structure formation (Loeb & Barkana 2001). The timeline of the reionisation process has been constrained by a series of observations undertaken over the last two decades. Measurement of the optical depth to Thomson scattering of the cosmic microwave background (CMB) radiation by the Planck team indicates a mid-point at $z = 7.7$ (Planck Collaboration et al. 2020). This is supported by a census of Lyα emitting galaxies at high redshift suggesting that the intergalactic medium (IGM) has a significant neutral hydrogen fraction ($x_{HI} \sim 50$ per cent) at $z \sim 7.5$ (see Ouchi et al. 2020 for a review). Moreover, the redshift-dependent flux seen in the Lyα forest of quasar spectra implies a nearly fully ionised IGM and hence that the reionisation process is effectively complete by $z \simeq 6$ (e.g., Fan et al. 2006; McGreer et al. 2015).

However, the nature of the sources responsible for cosmic reionisation is still a matter of debate. Over the last decade, thousands of star-forming galaxies (SFGs) at $z > 6$ have been detected in deep *Hubble Space Telescope* (*HST*) imaging surveys (e.g., Bouwens et al. 2015a; Finkelstein et al. 2015; Oesch et al. 2018) and a popular view is that such sources provide the major contribution to reionisation (e.g., Bouwens et al. 2015b; Robertson et al. 2015; Stanway et al. 2016; Dayal & Ferrara 2018). However, if all SFGs contribute equally, (i) the ultraviolet (UV) luminosity function of $z > 6$ galaxies must extend to intrinsically feeble systems with $M_{UV} \simeq -13$, and (ii) the fraction of ionising radiation that escapes into the IGM (the so-called 'escape fraction', f_{esc}) must be as high as $\simeq 20$ per cent (see Stark 2016 for a review). These requirements can be alleviated if rarer, more luminous systems make a more significant contribution, as suggested by the claimed rapid decline of the neutral fraction of the IGM over $6 \lesssim z \lesssim 7.5$ (e.g., Naidu et al. 2020). A possible explanation for this sudden end to reionisation is that many luminous sources may host active galactic nuclei (AGN) with both harder radiation fields (e.g., Steidel et al. 2014; Stark et al. 2015; Feltre et al.

2016) and larger escape fractions ($f_{esc} \sim 75 - 100$ per cent; e.g., Cristiani et al. 2016; Grazian et al. 2018).

At present, there is only indirect evidence supporting the hypothesis of AGN activity in galaxies at $z > 6$. High ionisation UV emission lines (e.g., N V $\lambda\lambda$1238, 1243, C IV $\lambda\lambda$1548, 1550) have been detected in a handful of star-forming galaxies (e.g., Tilvi et al. 2016; Hu et al. 2017; Laporte et al. 2017; Mainali et al. 2018; Sobral et al. 2019; Endsley et al. 2021b; Onoue et al. 2021). Although many AGN have been found in SFGs at $z \sim 2 - 4$ (e.g., Hainline et al. 2011), it seems the limited number of corresponding reionisation-era systems with potential AGN signatures show very different properties. This may make it questionable to identify AGN in $z > 6$ systems using the predominant spectral features seen in $z \sim 2 - 4$ AGN. Specifically, SFGs in the reionisation era often display rest-frame optical emission lines with extremely high equivalent widths (EWs), with an average [O III]+Hβ EW $\simeq 700$ Å at $z \sim 7 - 8$ (Labbé et al. 2013; De Barros et al. 2019; Endsley et al. 2021a). Such intense lines are seldom seen in lower redshift SFGs with AGN (e.g., Tang et al. 2019). Likewise, $z > 6$ galaxies have very steep UV continuum slopes ($\beta < -2.0$; e.g., Bouwens et al. 2012, 2014; Finkelstein et al. 2012) indicating metal-poor stellar populations with little dust. On the other hand, AGN at $z \sim 2 - 4$ present much redder UV slopes ($\beta > -1$, Fig. 1; e.g., Hainline et al. 2011; Le Fèvre et al. 2019), presumably because they are hosted by more massive galaxies with increased dust extinction (e.g., Hainline et al. 2012). A key question is whether these differences suggest that the nature and properties of AGN evolve significantly between $z \sim 2 - 3$ and $z > 6$, and that a population of blue, extreme optical line emitting galaxies harbouring AGN are somehow more abundant in the reionisation era.

The above question has motivated us to search for examples of AGN activity in $z \simeq 1 - 3$ SFGs with blue UV slopes and extreme optical line emission. To accomplish this, we exploit our large spectroscopic survey of extreme [O III] emitting galaxies at $z = 1.3 - 3.7$ at rest-frame optical (Tang et al. 2019, hereafter T19) and UV wavelengths (Tang et al. 2021a,b, hereafter T21a; T21b), targeting selected systems for evidence of AGN activity using diagnostic UV and optical emission lines in the context of photoionisation models (e.g., Allen et al. 2008; Feltre et al. 2016; Jaskot & Ravindranath 2016; Nakajima et al. 2018; Hirschmann et al. 2019; Plat et al. 2019). This enables us to distinguish between spectra powered by AGN and massive stars. In this paper, we present the case of a $z = 3.212$ AGN with extremely large EW [O III] emission with a steep UV continuum slope whose properties are thus similar to SFGs in the reionisation era (e.g., Endsley et al. 2021a). Our ultimate goal is to build a statistical sample of such $z \simeq 1 - 3$ AGN which may guide future spectroscopic searches for AGN activity in the reionisation era using future facilities such as the *James Webb Space Telescope* (*JWST*) or new generation of 30 metre class telescopes which can target the relevant UV and optical nebular emission lines.

The organisation of this paper is as follows. We describe our target selection and the spectroscopic observations in Section 2. The emission line measurements and the associated line ratio diagnostics that support evidence of AGN activity are discussed in Section 3. Finally, we discuss the implications of our results for the contribution of AGN to the reionisation era in Section 4. We adopt a Λ-dominated, flat universe with $\Omega_\Lambda = 0.7$, $\Omega_M = 0.3$, and $H_0 = 70$ km s^{-1} Mpc^{-1}. All magnitudes in this paper are quoted in the AB system (Oke & Gunn 1983), and all EWs are quoted in the rest frame.
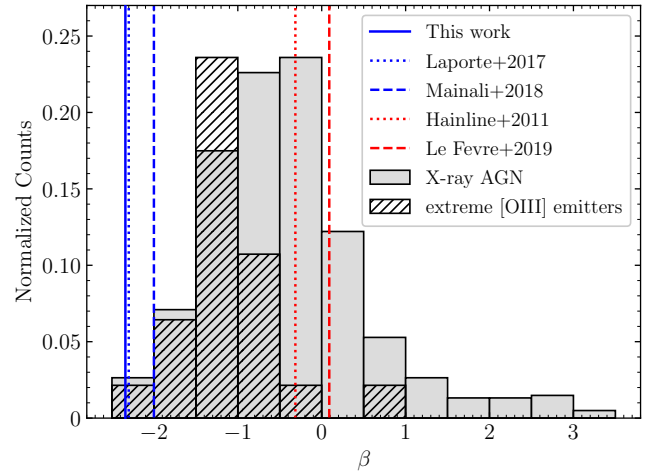
Figure 1. UV slope (β) distribution of all the X-ray AGN at $z = 1.3 - 3.7$ in the five CANDELS fields (606 objects; grey histogram) and that of the extreme [O III] emitting AGN (21 objects; black hatched histogram), of which the y-axis is rescaled to normalised counts. UV slopes are derived from the Barro et al. (2019) catalogs by cross-matching with *Chandra* catalogs in CANDELS fields (Xue et al. 2011, 2016; Nandra et al. 2015; Civano et al. 2016; Kocevski et al. 2018). The UV slopes of X-ray AGN at $z = 1.3 - 3.7$ are relatively red (median $\beta = -0.5$), consistent with the red UV slopes found in the stacked spectra of type II AGN at $z \sim 2 - 4$ in Hainline et al. (2011, red dotted line) and Le Fèvre et al. (2019, red dashed line), while the extreme [O III] emitting AGN show bluer UV slopes (median $\beta = -1.0$). On the other hand, the N V emitting AGN at $z > 7$ (Laporte et al. 2017, blue dotted line; Mainali et al. 2018, blue dashed line) and the $z = 3.21$ AGN studied in this paper, UDS-24561 (blue solid line), have much bluer UV slopes of $\beta < -2.0$.

2 OBSERVATIONS

In this work, we aim to locate and study the rest-frame UV and optical spectra of AGN with extremely large EW [O III] line emission and blue UV slopes. Our candidates will be chosen from a parent sample of extreme [O III] emitting AGN at $z = 1.3 - 3.7$. We describe the preselection of targets in Section 2.1, and the spectroscopic observations in Section 2.2, 2.3, and 2.4.

2.1 Pre-selection of extreme line emitting AGN with blue UV continuum slopes at z = 1.3 − 3.7

The first step of this study is to locate AGN candidates with extreme EW [O III] line emission and blue UV slopes for spectroscopic follow-up. In T19, we discuss the selection of a sample of extreme [O III] emitting objects at $z = 1.3 - 3.7$ in the Cosmic Assembly Near-infrared Deep Extragalactic Legacy Survey (CANDELS) fields (Grogin et al. 2011; Koekemoer et al. 2011) and their near-infrared (rest-frame optical) spectra. We direct the reader to T19 for details. In brief, extreme [O III] emitters were selected to have large rest-frame [O III] $\lambda\lambda$4959, 5007 EWs with values $\simeq 300 - 3000$ Å chosen to match the range common in reionisation-era sources (e.g., Endsley et al. 2021a). The [O III] EWs were inferred from *HST* grism spectra (at $z = 1.3 - 2.4$; T19) or the K-band flux excess (at $z = 3.1 - 3.7$; Tang et al. in preparation) using the 3D-HST catalogs (Brammer et al. 2012; Skelton et al. 2014; Momcheva et al. 2016).

To identify which are AGN we cross-match our $z = 1.3 - 3.7$ extreme [O III] emitter sample to deep *Chandra* X-ray source catalogues in the All-Wavelength Extended Groth Strip International Survey

(AEGIS; Nandra et al. 2015), the Cosmic Evolution Survey (COS-MOS; Civano et al. 2016), the Great Observatories Origins Deep Survey North (GOODS-N; Xue et al. 2016) and South (GOODS-S; Xue et al. 2011), and the Ultra Deep Survey (UDS; Kocevski et al. 2018) fields. The *Chandra* X-ray data used in the five CANDELS fields were reduced following the prescription described in Laird et al. (2009) and Nandra et al. (2015). The depths of the X-ray data are 800 ks in AEGIS, 160 ks in COSMOS, 2 Ms in GOODS-N, 4 Ms in GOODS-S, and 600 ks in UDS, resulting in hard band ($2 - 10$ keV) flux limits (over > 1 per cent of the survey area) of 2.5×10^{-16}, 1.8×10^{-15}, 5.9×10^{-17}, 5.5×10^{-17}, and 6.5×10^{-16} erg s^{-1} cm^{-2}, respectively. We match the coordinates of the extreme [O III] emitting objects (from the 3D-HST catalogs) to the X-ray source catalogs using a 1.0 arcsec search radius. There are 21 sources in our sample found to have X-ray counterparts within 1.0 arcsec.

We next examine whether the X-ray luminosities (L_X) of the 21 sources are consistent with those of X-ray AGN, which typically have $L_X \gtrsim 10^{42}$ erg s^{-1} at rest-frame $2 - 10$ keV. The X-ray luminosities of our sources were estimated by fitting the X-ray spectra assuming a power law with index $\Gamma = 1.7 - 1.8$ for intrinsic AGN spectra (AEGIS: Buchner et al. 2015; COSMOS: Marchesi et al. 2016; GOODS-N: Xue et al. 2016; GOODS-S: Xue et al. 2011; UDS: Kocevski et al. 2018). The absorption corrected rest-frame $2 - 10$ keV luminosities ($L_{2-10 \text{ keV}}$) of the 21 X-ray extreme [O III] emitting sources in our sample range from 1.1×10^{42} to 1.3×10^{45} erg s^{-1}. Since all the 21 sources have $L_{2-10 \text{ keV}} > 10^{42}$ erg s^{-1}, each is consistent with being an AGN.

The UV slope distribution of the 21 extreme [O III] emitting AGN at $z = 1.3 - 3.7$ is compared in Fig. 1 (black hatched histogram) to that of the total X-ray AGN sample in the CANDELS fields (grey histogram). Although extreme [O III] emitting AGN have relatively red (median $\beta = -1.0$) UV slopes, they are on average bluer than those of the total X-ray AGN sample (median $\beta = -0.5$). As the AGN continuum should not contribute significantly at rest-frame UV wavelengths (Assef et al. 2010), it appears that the host galaxies of extreme [O III] emitters are less dusty or more metal-poor than those of the majority of AGN at $z \sim 1 - 3$.

Our goal in this paper is to identify AGN at intermediate redshifts that are similar to the $z \simeq 7 - 9$ systems thought to harbour AGN in Laporte et al. (2017) and Mainali et al. (2018). Those objects are characterised by even bluer UV continuum slopes ($\beta < -2.0$; Fig. 1) and very large [O III]+Hβ EWs (> 900 Å in rest-frame) inferred from their extremely red *Spitzer*/IRAC $[3.6] - [4.5]$ colours. Among the 21 sources in our sample, only one object, UDS-24561 (R.A. $= 02:17:44.462$, Decl. $= -05:11:38.25$; Fig. 2), satisfies the joint criteria of $\beta < -2.0$ and rest-frame EW$_{\text{[OIII]+H}\beta} > 900$ Å. By measuring the emission lines shown in the low resolution ($R = 130$) *HST* grism spectrum (Momcheva et al. 2016; see Section 3.1), the estimated spectroscopic redshift of UDS-24561 is $z = 3.21$. We now examine this source in greater detail.

The multi-wavelength spectral energy distribution (SED) of UDS-24561 is presented in Fig. 3, which is extracted from the Skelton et al. (2014) photometry catalogs. This object is extremely luminous with absolute UV magnitude $M_{\text{UV}} = -22.4$, i.e., about five times brighter than the characteristic M^*_{UV} at $z \sim 3$ ($M^*_{\text{UV}} \simeq -20.6$; see Parsa et al. 2016, and references therein). The UV continuum slope of UDS-24561 is $\beta = -2.34$ and was computed by fitting a power law ($f_\lambda \propto \lambda^\beta$) to the broadband fluxes at rest-frame $1250 - 2600$ Å (Calzetti et al. 1994). The intense K-band flux excess indicates a large rest-frame [O III]+Hβ EW ($\simeq 1300$ Å; see Section 3.1 for more accurate measurements). Both properties are comparable to those of the putative AGN at $z \simeq 7 - 9$ discussed by Laporte et al. (2017)

and Mainali et al. (2018). The absorption corrected $L_{2-10 \text{ keV}}$ of this object in the Kocevski et al. (2018) catalog is 2.75×10^{44} erg s^{-1}, indicating that it is extremely luminous. We obtained the optical and near-infrared (rest-frame UV and optical) spectra of UDS-24561 via ground-based observations and *HST* archival data. We discuss the spectroscopic observations in the following subsections.

2.2 MMT/Binospec spectroscopy

The optical spectrum of UDS-24561 was obtained using the multi-slit spectrograph Binospec (Fabricant et al. 2019) on the MMT in order to measure the rest-frame UV emission lines. We designed one mask in the CANDELS/UDS field (centered at R.A. $= 02:17:26.8$ and Decl. $= -05:17:36$, with position angle PA $= -81°$) primarily targeting on UDS-24561. We filled the mask with non-AGN extreme [O III] emitting galaxies at $z = 1.3 - 3.7$, thereby continuing an on-going survey targeting rest-frame UV metal emission lines (T21a) and the Lyα emission line (T21b) in these systems. We observed this mask between 2020 October and November with a total on-target integration time of 28800 seconds during average seeing of 0.9 arcsec. Optical spectra of the targets were taken using the 270 lines mm^{-1} grism blazed at 5.5°, with wavelength coverage from 3850 to 9000 Å. The slit width was set to 1.0 arcsec, which results in a spectral resolution of $R = 1340$. This mask contains two slit stars to compute the absolute flux calibration, and we also observed spectrophotometric standard stars at a similar airmass in order to correct the instrument response.

The Binospec spectra were reduced using the publicly available data reduction pipeline[1] (Kansky et al. 2019). The pipeline performs flat-fielding, wavelength calibration, sky subtraction, and then the 2D spectra extraction. We created 1D spectra from the reduced 2D spectra using a boxcar extraction, with the extraction aperture matched to the spatial profile of the object. The atmospheric extinction and instrumental response were corrected using the sensitivity curve derived from observations of standard stars. We performed slit loss correction following the similar procedures in T19. We derived the spatial profile of each target from its *HST* F814W postage stamp, and computed the fraction of the light within the slit to that of the total spatial profile. The flux of each spectrum was then divided by the in-slit light fraction measured for each object. Finally, the absolute flux calibration was performed using observations of slit stars, by comparing the slit-loss corrected count rates of slit star spectra with the flux in the Skelton et al. (2014) catalogues.

2.3 Keck/MOSFIRE spectroscopy

We also obtained a near-infrared spectrum for UDS-24561 using the Multi-object Spectrometer for Infrared Exploration (MOSFIRE; McLean et al. 2012) on the Keck I telescope. We designed one multi-slit mask (centered at R.A. $= 02:17:41.25$ and Decl. $= -05:12:52.26$, with position angle PA $= 71°$) which primarily targets on UDS-24561. The mask was filled with non-AGN extreme [O III] emitting galaxies at $z = 2.1 - 3.7$ following the survey strategy discussed in T19. We observed this mask on 2021 March 3 and 4, with a total on-target integration time of 2880 seconds and an average seeing of 0.8 arcsec. The spectra were taken in the K-band with wavelength coverage from 1.954 to 2.397 μm, aiming to measure the Hβ and [O III] emission lines for UDS-24561, as well as Hα or Hβ and [O III] emission lines for the fillers. The slit width was set to 0.7 arcsec,

---

[1] https://bitbucket.org/chil_sai/binospec

resulting in a spectral resolution of $R = 3610$. We also placed two slit stars on the mask for absolute flux calibration, and observed A0V stars to derive the response spectra and correct for telluric absorption.

The MOSFIRE spectra were reduced using the publicly available PYTHON-based data reduction pipeline[2] (DRP). The pipeline performs flat-fielding, wavelength calibration, and background subtraction before 2D spectra extraction. We created 1D spectra from the reduced 2D spectra using a boxcar extraction. The telluric absorption and instrumental response were corrected using observations of A0V stars. Slit loss correction of each target was performed using the in-slit light fraction computed from its *HST* F160W image. We then performed the absolute flux calibration using observations of slit stars, by comparing the observed fluxes of star spectra with the broadband photometry.

2.4 *HST* WFC3/G141 spectroscopy

In addition to the MMT/Binospec and the Keck/MOSFIRE *K*-band observations, we use the emission line measurements in the *HST* Wide Field Camera 3 (WFC3) G141 slitless grism spectrum of UDS-24561 from the 3D-HST survey, which is described in detail in Momcheva et al. (2016). The *HST* WFC3/G141 grism has spectral coverage from 1.1 to 1.7 μm (corresponding to ground-based *J* and *H* bands) and a spectral resolution of $R = 130$. The grism images were first reduced by removing satellites trails and earthshine, followed by flat-fielding and background subtraction. Then the exposures were combined by interlacing into output mosaic images used for the spectral extractions. After that a contamination model was created to account for overlapping spectra due to neighboring sources, and the 2D spectra of individual objects were extracted from the interlaced mosaic images and contamination were subtracted. Finally, the 1D spectra were extracted using the optimal extraction procedures (Horne 1986).

3 RESULTS

The luminous X-ray detection of UDS-24561 reveals that this system hosts an AGN. In this section, we explore the spectral properties of UDS-24561 in more detail with the optical and near-infrared spectra described in Section 2. We first present the emission line identification and measurements (Section 3.1), then compare the observed line ratios to line diagnostics developed from photoionisation models to examine their capability of identifying the nature of the ionising sources (Section 3.2).

3.1 Emission line measurements

The rest-frame UV and optical spectra of UDS-24561 are shown in Fig. 4. We visually inspect the spectra and identify a number of emission lines including O VI $\lambda\lambda 1032, 1038$, Ly$\alpha$, C IV $\lambda\lambda 1548, 1550$, He II $\lambda 1640$, Mg II $\lambda\lambda 2976, 2803$, [O II] $\lambda\lambda 3727, 3729$, [Ne III] $\lambda 3869$, Hβ, [O III] $\lambda 4959$, [O III] $\lambda 5007$, and tentatively Si $\lambda 1393$ ($\sim 2\sigma$), while N V $\lambda\lambda 1238, 1243$, Si $\lambda 1402$, O III] $\lambda\lambda 1661, 1666$, and C III] $\lambda\lambda 1907, 1909$ emission lines are not detected. The systemic redshift of UDS-24561 is determined using the line centers of non-resonant emission lines with spectral resolution $R > 1000$, i.e., He II $\lambda 1640$, [O III] $\lambda 4959$, and [O III] $\lambda 5007$ emission lines, resulting in $z_{sys} = 3.2124 \pm 0.0006$.
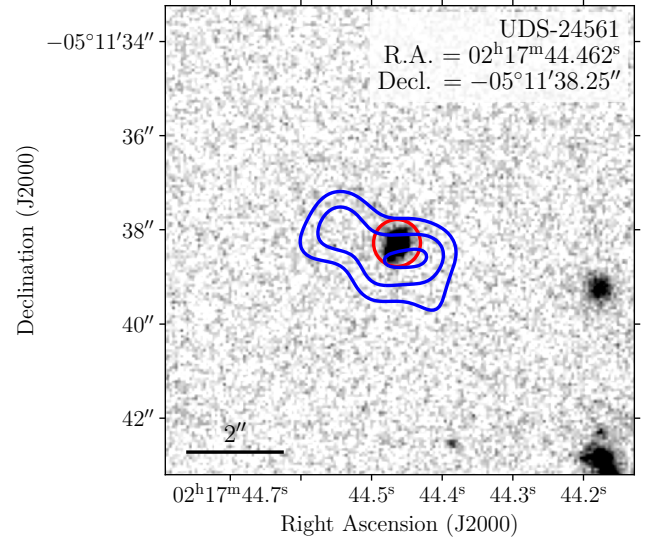

Figure 2. Rest-frame UV and X-ray imaging of UDS-24561. The black-white image shows the *HST* F814W (rest-frame UV) postage stamp ($10'' \times 10''$) of UDS-24561. The red circle shows the region centered on UDS-24561 with a radius of 0.5 arcsec. The blue contour overlaying the F814W imaging shows the full band ($0.5 - 10$ keV) deep *Chandra* X-ray imaging, with contour lines represent count levels of 1, 1.5, and 2. The *Chandra* X-ray source is consistent with the *HST* imaging, indicating that the X-ray emission comes from UDS-24561.
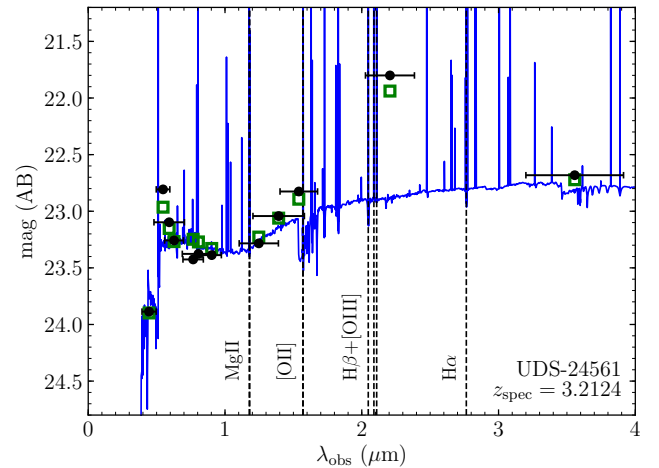

Figure 3. The spectral energy distribution of UDS-24561. Observed broadband photometry extracted from the Skelton et al. (2014) catalogs is shown as solid black circles. The best-fit SED model inferred from the Bayesian spectral energy distribution modeling and interpreting tool BEAGLE (Chevallard & Charlot 2016) are plotted by solid blue lines, and synthetic photometry is presented by open green squares. The SED of UDS-24561 shows a blue UV slope ($\beta = -2.34$) and an intense *K*-band flux excess indicating a large [O III]+Hβ EW ($\simeq 1300$ Å).

Emission line fluxes of UDS-24561 are determined from the extracted 1D spectra. For He II λ1640, we fit the line profile with a single Gaussian to derive the line flux. For O VI $\lambda\lambda$1032, 1038 and C IV $\lambda\lambda$1548, 1550 doublets, we fit two Gaussians to derive the line flux of each individual component of the doublet. For [O III] λ5007, we fit two Gaussians with a broad and a narrow component since the emission line cannot be well fitted by a single Gaussian, and the narrow component was used to compute the systemic redshift. The Lyα emission line of UDS-24561 shows a double-peak profile and we fit four Gaussians, so that both blue and red Lyα components can be fitted by broad and a narrow components. For Hβ and [O III] λ4959, we calculate the line flux using direct integration instead of fitting Gaussians since these two emission lines are contaminated by sky lines and thus have low signal-to-noise ratio (S/N < 4). We also use direct integration to compute the flux of the tentative Si λ1393 emission line (S/N = 2). For the blended Mg II $\lambda\lambda$2976, 2803, [O II] $\lambda\lambda$3727, 3729 doublets and [Ne III] λ3869 which lie in the *HST* grism spectrum, we use the line flux provided in the Momcheva et al. (2016) catalogs. Previous studies show that the line fluxes measured from *HST* grism spectra are consistent with the values measured from ground-based observations (e.g., Kriek et al. 2015; T19). For the non-detected N V $\lambda\lambda$1238, 1243, Si λ1402, O III] $\lambda\lambda$1661, 1666, and C III] $\lambda\lambda$1907, 1909 lines, we derive 3σ upper limits by summing the error spectrum in quadrature over ~ 200 km/s, a value consistent with the upper bound of line widths found for UV metal lines (e.g., Stark et al. 2014).

We next compute the corresponding rest-frame EW for each emission line. Robust measurements of continuum flux are required to compute EWs. For emission lines (except for Lyα) lying in the MMT/Binospec spectrum which shows bright continuum emission (S/N > 5), we derive the continuum flux density in a clean window of ±150 Å near the emission line in the extracted 1D spectrum. For Lyα we estimate the continuum flux by averaging the flux over rest-frame $1270 - 1300$ Å in order to avoid contamination from nearby features (H I absorption blueward of Lyα, and N V, Si II redward of Lyα; e.g., Matthee et al. 2021). For Mg II, [O II], and [Ne III] in the *HST* grism spectrum, we use the EWs provided in the Momcheva et al. (2016) catalogs. We also compute these EWs by measuring the continuum flux from the grism spectrum and they are in agreement with the EWs provided by the 3D-HST team. For Hβ and [O III] in the Keck/MOSFIRE spectrum where a bright continuum emission is not available, we derive the continuum flux by subtracting the emission line fluxes from the total K-band flux. We summarise the emission line measurements of UDS-24561 in Table 1, including the deconvolved FWHMs (after subtracting the instrument resolution in quadrature), line fluxes, and EWs.

The most prominent emission line detected in the spectra of UDS-24561 is [O III] λ5007, with EW = 935 ± 167 Å. The total [O III]+Hβ EW measured from spectrum is 1298 ± 193 Å, which is consistent with the value inferred from the K-band flux excess (EW $\simeq 1300$ Å; Fig. 3). Such intense optical line emission is extremely rare at $z \sim 0-3$, but becomes more common in the reionisation era (e.g., 20 per cent of the $z \simeq 7$ population has [O III]+Hβ EW > 1200 Å; Endsley et al. 2021a).

The [O III] doublets and Hβ emission lines show extended profiles (Fig. 4), and the [O III] λ5007 line is best fitted by two Gaussians: a narrow component with FWHM = 154 ± 21 km/s and a broad component with FWHM = 977 ± 131 km/s (Fig. 5). A broad line could be due to merger activity, emission from the broad line region of an AGN or AGN-driven outflows. We note that the *HST* image of UDS-24561 (Fig. 2) does not indicate any evidence of merger activity. Moreover, the broad [O III] line width of UDS-24561 is

somewhat less than the typical line width seen in AGN broad line regions (FWHM $\gtrsim 2000$ km/s). Although supernova feedback or shock-ionised outflows can also produce broad line emission, the FWHMs ($\sim 300 - 600$ km/s; e.g., Veilleux et al. 2005; Freeman et al. 2019; Matthee et al. 2021) are smaller than that of UDS-24561. On the other hand, the broad optical line velocity of UDS-24561 is in agreement with those of AGN outflows (e.g., Förster Schreiber et al. 2014; Genzel et al. 2014; Leung et al. 2017, 2019). We estimate a lower limit to the broad [O III] λ5007/Hβ ratio using the total flux of Hβ (since we cannot accurately decouple the broad and narrow emission components for Hβ). The line ratio (> 9.3 at 3σ) is consistent with those of AGN (e.g., Coil et al. 2015; Azadi et al. 2017) and greater than the maximum ratio predicted by starburst models (e.g., Kauffmann et al. 2003; Kewley et al. 2013). Thus we conclude that the broad optical lines of UDS-24561 likely originate from an AGN-driven outflow.

The Lyα emission line of UDS-24561 shows a more complex profile (Fig. 6). The emission is double-peaked, and both the blue and red Lyα components show extended emission line features. None of the blue and red Lyα component could be fitted by a single Gaussian. However, we find that each Lyα component is best fitted by two Gaussians including a narrow (FWHM = $87 - 513$ km/s) and a broad (FWHM = $814 - 987$ km/s) component, indicating the blue and red wings extending to maximal velocities of -2000 km/s and $+1600$ km/s (Fig. 6). The broad wing features, together with the small velocity offset of red peak Lyα with respect to the systemic redshift ($\Delta v_{\mathrm{Ly}\alpha} = +141 \pm 76$ km/s), suggest conditions that are conducive to leaking Lyα photons (e.g., Erb et al. 2014; Hashimoto et al. 2015; Henry et al. 2015; Martin et al. 2015). The total Lyα luminosity and EW of UDS-24561 are extremely large, with $L_{\mathrm{Ly}\alpha} = 2.8 \pm 0.3 \times 10^{44}$ erg s^{-1} and EW$_{\mathrm{Ly}\alpha} = 436 \pm 45$ Å, which the $L_{\mathrm{Ly}\alpha}$ is ~ 50 times the typical Lyα luminosity of LAEs at $z \sim 3$ ($L^*_{\mathrm{Ly}\alpha} \simeq 10^{42.7}$ erg s^{-1}; e.g., Sobral et al. 2018a). Such luminous $L_{\mathrm{Ly}\alpha}$ and L_{UV} (~ 5 times the typical UV luminosity at $z \sim 3$; Parsa et al. 2016), together with the blue UV slope, are consistent with the picture that the physics of accretion discs of massive black holes can destroy the dust in very luminous systems and allow Lyα and UV photons to escape (e.g., Sobral et al. 2018b).

Intense high ionisation emission lines from O VI,[3] Si IV λ1393, C IV, and He II have also been detected in the rest-frame UV spectrum of UDS-24561 (Fig. 4), suggesting a hard ionising radiation field powered by an AGN (e.g., Feltre et al. 2016; Volonteri et al. 2017). Unlike Lyα, Hβ, or [O III], we do not detect significant broad emission features for these high ionisation lines. As the UV line fluxes are relatively fainter, it could be more difficult to detect broad emission components and deeper spectra are required to measure such features. The line profile of He II is narrow and the line width is comparable to the instrument resolution. We estimate the 3σ upper limit of the deconvolved FWHM < 216 km/s for He II, which is consistent with the FWHM of the narrow [O III] λ5007 emission line (154 ± 21 km/s). Individual components of the O VI and C IV doublets show wider FWHMs (= $340 - 499$ km/s), which could be due to the resonant nature of these emission lines.

The O VI, Si IV λ1393, C IV, and He II EWs derived from the spectrum of UDS-24561 are EW$_{\mathrm{OVI}} = 16.2 \pm 2.6$ Å, EW$_{\mathrm{SiIV}\lambda1393} = 1.1 \pm 0.5$ Å, EW$_{\mathrm{CIV}} = 27.4 \pm 4.0$ Å and EW$_{\mathrm{HeII}} = 5.3 \pm 1.3$ Å. Significant stellar or interstellar absorption features are not seen in the vicinity of O VI, Si IV λ1393, or C IV emission lines, although

---

[3] The spectral resolution of MMT/Binospec allows us to deblend Lyβ (at rest-frame 1025.73 Å) and O VI $\lambda\lambda$1032, 1038 lines

Line	λ_{rest} (Å)	FWHM (km/s)	Flux (10^{-17} erg s^{-1} cm^{-2})	EW (Å)
O VI	1031.91	354 ± 54	6.32 ± 1.27	8.6 ± 1.7
...	1037.61	499 ± 99	5.56 ± 1.46	7.6 ± 2.0
Ly$\alpha_{b,n}$	1215.67[a]	87 ± 11	13.10 ± 2.17	19 ± 3
Ly$\alpha_{b,b}$	1215.67[b]	814 ± 269	11.45 ± 4.20	16 ± 6
Ly$\alpha_{b,t}$	1215.67[c]	...	24.55 ± 4.72	35 ± 7
Ly$\alpha_{r,n}$	1215.67[d]	513 ± 23	195.8 ± 21.8	280 ± 31
Ly$\alpha_{r,b}$	1215.67[e]	987 ± 168	84.07 ± 21.78	120 ± 31
Ly$\alpha_{r,t}$	1215.67[f]	...	279.9 ± 30.8	401 ± 44
N V	1238.82	...	< 1.46	< 2.1
...	1242.80	...	< 1.43	< 2.0
Si IV	1393.76	...	0.74 ± 0.34	1.1 ± 0.5
...	1402.77	...	< 1.43	< 2.1
C IV	1548.19	440 ± 65	9.74 ± 1.62	18.2 ± 3.0
...	1550.77	340 ± 83	4.93 ± 1.39	9.2 ± 2.6
He II	1640.42	< 216	2.60 ± 0.64	5.3 ± 1.3
O III]	1660.81	...	< 1.15	< 2.3
...	1666.15	...	< 1.07	< 2.2
C III]	1908[g]	...	< 3.30	< 9.7
Mg II	2798[h]	...	8.36 ± 1.18	63 ± 10
[O II]	3728[i]	...	14.94 ± 0.65	172 ± 12
[Ne III]	3870.16	...	3.12 ± 0.70	27 ± 7
Hβ	4862.69	...	4.76 ± 2.08	69 ± 30
[O III]	4960.30	...	21.51 ± 6.66	294 ± 91
[O III]$_n$	5008.24[j]	154 ± 21	9.28 ± 1.90	129 ± 26
[O III]$_b$	5008.24[k]	977 ± 131	58.05 ± 11.90	805 ± 165
[O III]$_t$	5008.24[l]	...	67.38 ± 12.05	935 ± 167

Table 1. Rest-frame UV and optical emission line measurements of UDS-24561 at $z = 3.2124$, including the deconvolved FWHM (Column 3), line flux (Column 4), and rest-frame EW (Column 5). For non-detected N V, O III], and the blended C III] lines, 3σ upper limits are provided.
[a] Narrow component of the blue peak of Lyα.
[b] Broad component of the blue peak of Lyα.
[c] Total of the blue peak of Lyα.
[d] Narrow component of the red peak of Lyα.
[e] Broad component of the red peak of Lyα.
[f] Total of the red peak of Lyα.
[g] Total of the blended C III] $\lambda\lambda$1907, 1909.
[h] Total of the blended Mg II $\lambda\lambda$2796, 2803.
[i] Total of the blended [O II] $\lambda\lambda$3727, 3729.
[j] Narrow component of [O III] λ5007.
[k] Broad component of [O III] λ5007.
[l] Total of [O III] λ5007.

we cannot rule out a modest level of absorption and hence these emission line EWs could be even larger. The majority of metal-poor SFGs do not present such large EWs (e.g., Erb et al. 2010; Vanzella et al. 2016; Senchyna et al. 2017, 2019; Berg et al. 2018, 2019; Du et al. 2020), except a few sources show similar C IV EWs (Stark et al. 2015; Mainali et al. 2017; Vanzella et al. 2017). On the contrary, the high ionisation line EWs of UDS-24561 are comparable to the values measured in AGN (e.g., Hainline et al. 2011; Le Fèvre et al. 2019; Mignoli et al. 2019; Grazian et al. 2020; Saxena et al. 2020). Using the available UV emission line ratios of UDS-24561, we will test whether the line diagnostics developed to identify ionising sources are capable of distinguishing between spectra powered by blue, extreme optical line emitting AGN and massive stars in Section 3.2.

3.2 Emission line diagnostics

Various diagnostics involving rest-frame UV emission lines have been developed to determine the nature of the ionising sources (i.e., star formation, nuclear activity, or shocks) using photoionisation models (e.g., Feltre et al. 2016; Nakajima et al. 2018; Hirschmann et al. 2019). The emission line measurements of UDS-24561 provide a unique opportunity to examine the capability of the line diagnostics in identifying AGN in extreme optical line emitting systems with blue UV slopes. Since blue, extreme [O III] emitting sources are common at $z > 7$ (e.g., Smit et al. 2015; Endsley et al. 2021a), and UV emission lines will likely remain the most useful diagnostics for studies of the most distant galaxies, our present analysis will provide useful insight into identifying AGN in the reionisation era.

For emission line ratios predicted from photoionisation models, we consider the SFG models taken from Gutkin et al. (2016) and the latest version of Feltre et al. (2016) AGN narrow line region models presented in Mignoli et al. (2019). The nebular emission of both models is computed using the photoionisation code CLOUDY (Ferland et al. 2013). In this work, we focus on emission line ratios involving O III] $\lambda\lambda$1661, 1666 and C IV $\lambda\lambda$1548, 1550, He II λ1640. Since the ionising spectra of metal-poor hot stars decline rapidly around 50 eV while those of AGN extend to much higher energies (e.g., Figure 1 in Feltre et al. 2016), the oxygen atoms in AGN are expected to be largely triply ionised while C IV and He II emission is strong compared to SFGs. We thus expect a decrease in O III] to He II or C IV ratio in AGN, and these line ratios can be used to determine the ionising sources.

In the left panel of Fig. 7, we show the C IV/He II versus O III]/He II diagnostic for both nebular emission from photoionisation models (magenta squares: AGN; cyan stars: SFG) and observations (red solid symbols: AGN; blue open symbols: SFG). Photoionisation models and observations at $z \simeq 0 - 4$ in literature indicated that narrow-line AGN reach smaller C IV/He II ratios (< 7) as well as smaller O III]/He II ratios at fixed C IV/He II compared to non-AGN SFGs. The line ratios of the blue, extreme [O III] emitting AGN, UDS-24561, are also consistent with this picture. Using the AGN models in Feltre et al. (2016), we find that the UV line ratios of UDS-24561 are best reproduced by an ionising spectrum with a slope of $\alpha \simeq -2.0$ (assuming $f_\nu \propto \nu^\alpha$ at rest-frame wavelength $\lambda < 912$ Å) and a very large ionisation parameter ($\log U \simeq -1.0$). We also notice that the line ratios of UDS-24561 are located in the AGN − SFG region, implying that they can be reproduced by a few SFG models as well. However, for non-AGN SFG models to reproduce the line ratios of UDS-24561, much lower ionisation parameters ($\log U < -3.0$) and larger gas-phase metallicities ($Z > Z_\odot$) are required, both conditions allowing to reduce the emissivity of O III] relative to He II. SFG models with such conditions are not able to reproduce the large C IV EWs seen in AGN.[4]

The flux ratio of O III] and C IV provides another way to determine the ionising sources (e.g., Mainali et al. 2017). In the right panel of Fig. 7 we show the He II/C IV versus O III]/C IV diagnostic. The O III]/C IV ratio of UDS-24561 is consistent with those of UV-selected AGN at similar redshift in literature (Hainline et al. 2011; Alexandroff et al. 2013; Le Fèvre et al. 2019), which are larger

---

[4] Using the BEAGLE tool (Chevallard & Charlot 2016) which adopted the latest version of stellar population synthesis code in Bruzual & Charlot (2003) and the nebular emission models from Gutkin et al. (2016), the largest predicted C IV EW for models with $\log U < -3.0$ and $Z > Z_\odot$ is only 1 Å assuming a constant star formation history, which is significantly smaller than the C IV EWs of AGN.
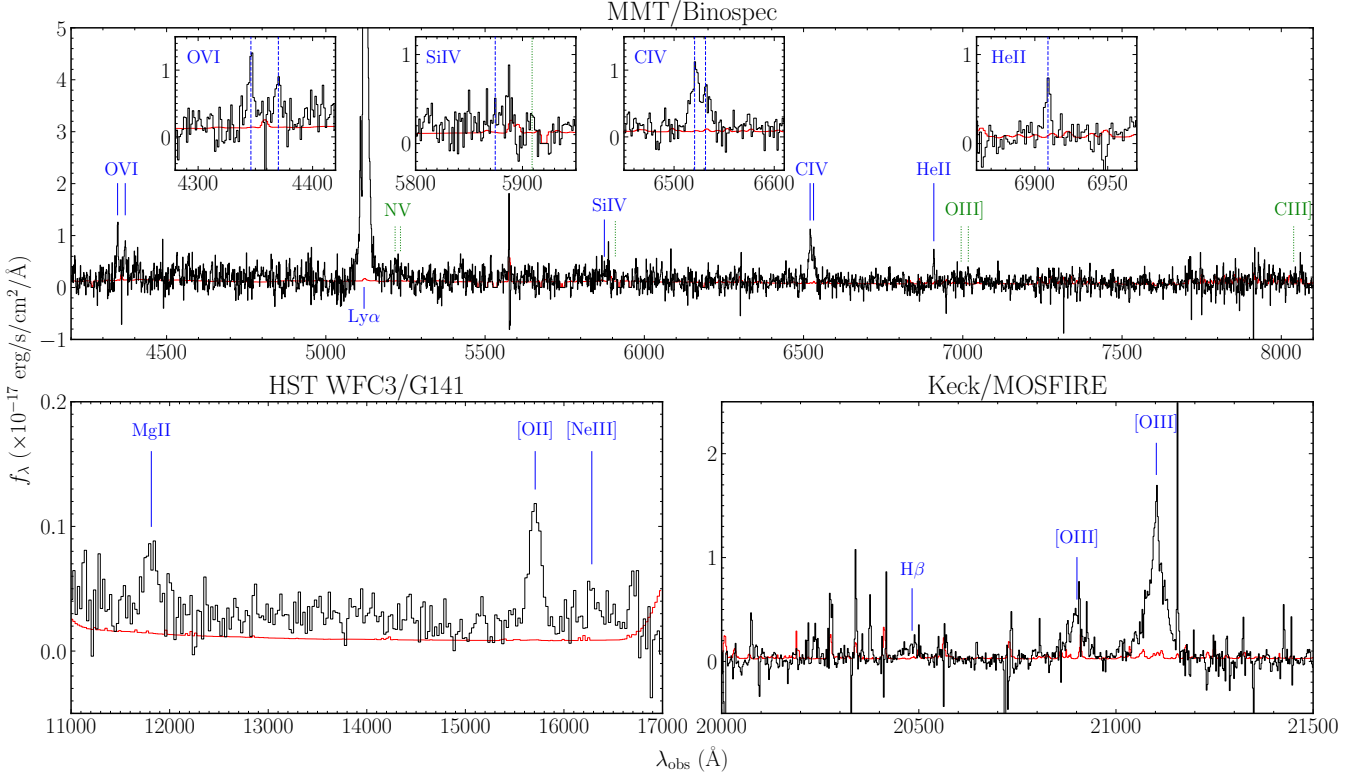
Figure 4. Rest-frame UV and optical spectra of UDS-24561. MMT/Binospec, *HST* WFC3/G141, and Keck/MOSFIRE spectra are shown in the top, the bottom left, and the bottom right panel, respectively. The black and red solid histograms represent the observed flux and 1σ uncertainty. Detected emission lines including O VI $\lambda\lambda1032, 1038$, Lyα, Si IV $\lambda1393$ (tentatively), C IV $\lambda\lambda1548, 1550$, He II $\lambda1640$, blended Mg II $\lambda\lambda2976, 2803$, blended [O II] $\lambda\lambda3727, 3729$, [Ne III] $\lambda3869$, Hβ, [O III] $\lambda4959$, and [O III] $\lambda5007$ are marked by blue solid lines. Predicted positions of non-detected N V, Si IV $\lambda1402$, O III], and C III] lines are marked by green dotted lines. In the top panel, we also show the zoom-in spectra of O VI, Si IV, C IV, and He II emission lines.

than the ratios of non-AGN metal-poor SFGs at fixed He II/C IV ratio. We also notice that the UV-blue AGN UDS-24561 appears to have smaller He II/C IV ratio compared to AGN with red UV continua at similar redshift in Hainline et al. (2011) and Le Fèvre et al. (2019). This may suggest different properties between these two populations (e.g., metallicity or dust content of the host galaxies, see Section 1). The results presented in Fig. 7 demonstrate that emission line diagnostics involving high ionisation lines such as C IV, He II, and O III] are applicable to identifying AGN in extreme optical line emitting galaxies with blue UV continua. Future spectroscopic observations of a larger statistical sample of such systems will help to confirm the capability of the UV diagnostics in determining the ionising sources of reionisation-era galaxies.

4 DISCUSSION

In the foregoing, we have demonstrated that, both from its detailed spectrum and X-ray luminosity, the extreme line emitting galaxy UDS-24561 contains an AGN. Yet it is also a close analogue of sources known to be common in the reionisation era. UDS-24561 displays a very blue UV slope ($\beta = -2.34$) and a large [O III]+Hβ EW (= 1298 Å). Rest-frame optical line emission appears to be prominent at $z \gtrsim 7$ (e.g., Labbé et al. 2013; De Barros et al. 2019; Endsley et al. 2021a) and 20 per cent of this population has extremely large [O III]+Hβ EW of > 1200 Å (Endsley et al. 2021a), similar to

the [O III]+Hβ EW of UDS-24561. The UV continuum slopes of the reionisation-era population ($\beta \simeq -2.0$) are also bluer than those of star-forming galaxies at lower redshifts (e.g., Bouwens et al. 2012, 2014; Finkelstein et al. 2012). In this section, we consider the implications of UDS-24561 for identifying AGN activity in reionisation-era galaxies and their contribution to the ionising background at $z > 6$.

UDS-24561 provides a detailed glimpse of a population of AGN that may become common in the reionisation era. Its distinct properties relative to more typical AGN at intermediate redshifts may be useful in locating AGN at very high redshift ($z > 6$), leading to a better understanding of their role in contributing to cosmic reionisation. This is further supported by the fact that extreme optical line emitting systems are likely effective ionising agents (e.g., Chevallard et al. 2018; Fletcher et al. 2019; T19; T21b).

Unfortunately, identifying AGN activity at $z \gtrsim 7$ with traditional means is likely to be difficult with current facilities. Current deep X-ray surveys do not have the sensitivity to locate individual examples. Consider, for example, an X-ray source with the same luminosity as UDS-24561. The full ($0.5 - 10$ keV), soft ($0.5 - 2$ keV), and hard band ($2 - 10$ keV) fluxes of UDS-24561 at $z = 3.2124$ are 3.01×10^{-15}, 0.59×10^{-15}, and 2.69×10^{-15} erg s^{-1} cm^{-2} (Kocevski et al. 2018), respectively. At $z = 7$ such a source would have X-ray fluxes of $= 5.84 \times 10^{-16}$, 1.14×10^{-16}, and 5.22×10^{-16} erg s^{-1} cm^{-2}, respectively, in the full, soft, and hard bands assuming a power-law index of $\Gamma = 1.7$ (Brightman et al. 2014). These fluxes are comparable to the 1σ sensitivity of the 600 ks deep *Chandra* X-ray
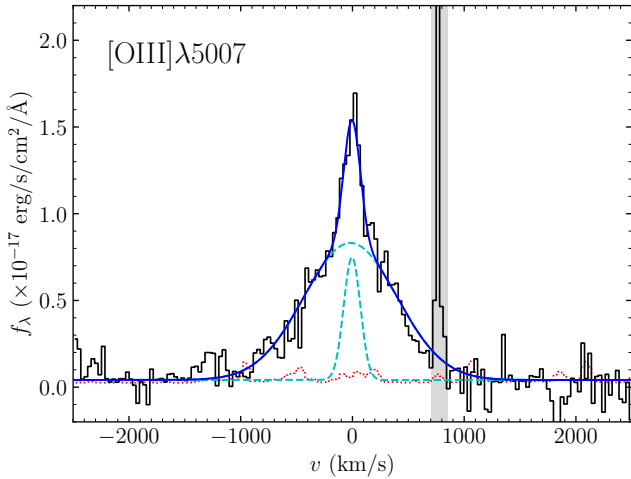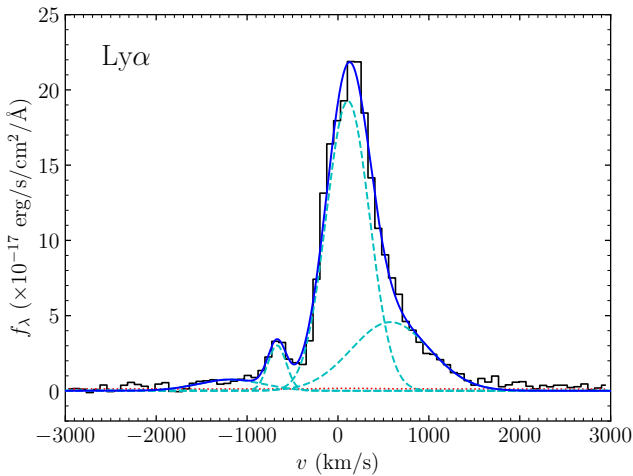
Figure 5. Observed [O III] λ5007 emission line of UDS-24561 and the best-fit line profile. The x-axis shows the velocity offset with respect to the systemic redshift. Observed flux and 1σ uncertainty are shown by the black solid histogram and the red dotted line. The grey shaded region marks the region that is strongly contaminated by sky line residuals. The [O III] λ5007 emission line is best fitted by a double-Gaussian profile (blue solid line), with a narrow component with FWHM = 154 ± 21 km/s and a broad component with FWHM = 977 ± 131 km/s (both shown by the cyan dashed lines).

Figure 6. Observed Lyα emission line of UDS-24561 and the best-fit line profile. The x-axis shows the velocity offset with respect to the systemic redshift. Observed flux and 1σ uncertainty are shown by the black solid histogram and the red dotted line. The Lyα emission line shows a double-peaked profile, and each of the blue peak and red peak Lyα line is best fitted by a double-Gaussian profile (a quadruple-Gaussian profile for the total Lyα emission, shown by the blue solid line), with a narrow component (FWHM = $87 - 513$ km/s) and a broad component (FWHM = $814 - 987$ km/s). Each of the single Gaussian component is shown by the cyan dashed line. The blue (red) wing feature extends to a maximal velocity of ~ -2000 km/s ($+1600$ km/s).

survey in the CANDELS/UDS field (4.4×10^{-16}, 1.4×10^{-16}, and 6.5×10^{-16} erg s^{-1} cm^{-2} in the full, soft, and hard band; Kocevski et al. 2018). Although the 4 Ms *Chandra* Deep Field-South survey reaches deeper flux limits (Xue et al. 2011), an individual AGN at $z = 7$ with $L_{2-10 \text{ keV}} \lesssim 6 \times 10^{43}$ erg s^{-1} would still be undetected. Not surprisingly, no X-ray counterparts have been seen in all the six luminous ($L_{\text{UV}} = 1.3 - 2.5 \times L_{\text{UV}}^*$) N V-emitting galaxies at $z = 6.5 - 9$ (Tilvi et al. 2016; Hu et al. 2017; Laporte et al. 2017; Mainali et al. 2018; Sobral et al. 2019; Endsley et al. 2021b). Future X-ray facilities will help accumulate larger AGN samples in the reionisation era (e.g., Vito et al. 2018).

Likewise the broad Hβ and [O III] emission lines of UDS-24561, which likely reflect AGN-driven outflows, cannot readily be revealed in $z \gtrsim 7$ spectra with current facilities. Detecting broad emission in individual lines requires relatively high resolution spectra ($R \gtrsim 1000$) of good quality (S/N > 5). Although the blended [O III]+Hβ luminosities and EWs of $z \sim 7 - 9$ systems can be estimated from the *Spitzer*/IRAC [3.6] − [4.5] colors (e.g., Labbé et al. 2013; Smit et al. 2014; De Barros et al. 2019; Endsley et al. 2021a), clearly broad emission cannot be discerned. As with studies of the diagnostic line ratios of [N II]/Hα or [S II]/Hα in the mid-infrared, rest-frame optical diagnostics of AGN activity at $z \gtrsim 7$ must await spectroscopy with *JWST*/NIRSpec.

Signs of AGN activity in the reionisation era can also be probed by rest-frame UV spectroscopy. The presence of high ionisation emission lines such as O VI or N V, and strong Mg II line emission suggest hard radiation fields that are likely powered by AGN. As discussed in Section 3.2 and earlier work (e.g., Alexandroff et al. 2013; Feltre et al. 2016; Laporte et al. 2017; Mainali et al. 2017; Nakajima et al. 2018; Hirschmann et al. 2019; Mignoli et al. 2019), UV line diagnostics are capable of characterising the shape of the ionising spectrum and hence distinguishing between AGN and star formation. However, this requires relatively high signal-to-noise ratio spectroscopy that can place key constraints on multiple high ionisation UV lines including C IV and He II.

We have argued in this paper that UDS-24561 may provide a possible template for estimating the abundance of $z \gtrsim 7$ galaxies hosting AGN if its combination of intense [O III] emission and blue UV continuum slopes is a key characteristic. Although simply a hypothesis at present given the paucity of examples, the similarity between the properties of UDS-24561 and candidate galaxies with AGN in the reionisation era is striking.

Recently, Naidu et al. (2020) interpreted a rapid conclusion of reionisation over $6 < z < 7.5$ in the context of an additional population of rarer, more massive galaxies. In their Model I, bright galaxies with $M_{\text{UV}} < 18$, which account for less than 5 per cent of the early population, are arranged to account for > 50 per cent of the reionising photon budget. Via this hypothetical model, the rapid evolution in the redshift-dependent neutral fraction x_{HI} in the IGM can be matched. Although clearly not an unique interpretation of the x_{HI} data, a possible physical explanation of such a mass-dependent contribution of ionising photons would be the late development of AGN in a subset of massive galaxies, each of which would have more powerful ionising capabilities.

As an illustration of this hypothesis in the context of UDS-24561, we can estimate the additional contribution of ionising photons arising if some proportion of sources with intense [O III] emission and blue UV continuum slopes have a 100 per cent escape fraction due to a powerful AGN. If, for example, 20 per cent of such luminous galaxies harbour AGN and the escape fraction assigned to this subset is $f_{\text{esc}} = 1$, and the remaining sources have $f_{\text{esc}} = 0.2$, AGN can readily supply the required energy budget of $50 - 60$ per cent
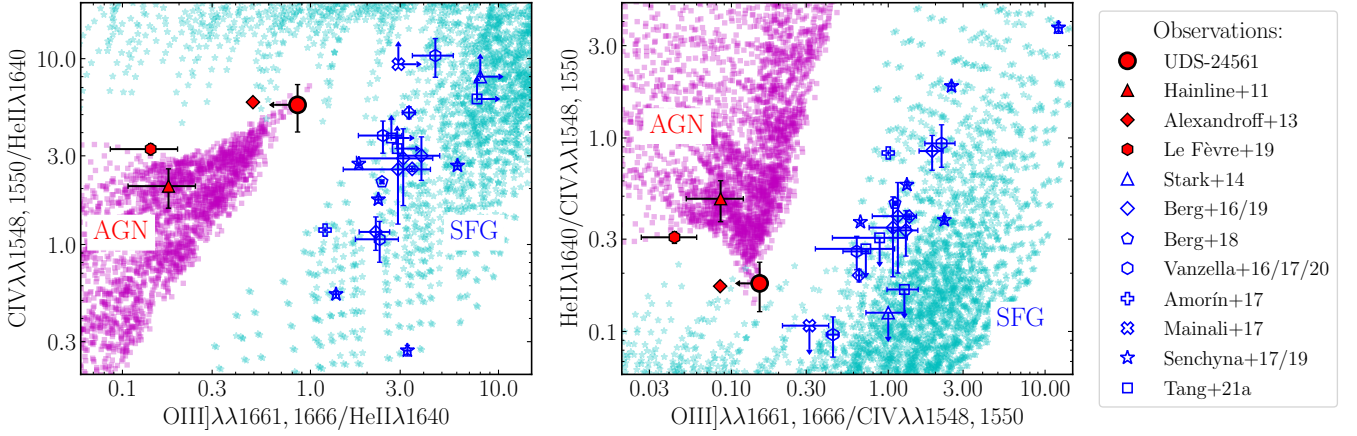
Figure 7. *Left:* C IV $\lambda\lambda$1548, 1550/He II λ1640 versus O III] $\lambda\lambda$1661, 1666/He II λ1640 diagnostic diagram (Feltre et al. 2016). *Right:* He II λ1640/C IV $\lambda\lambda$1548, 1550 versus O III] $\lambda\lambda$1661, 1666/C IV $\lambda\lambda$1548, 1550 diagnostic diagram (Mainali et al. 2017). Line ratios taken from photoionisation models are plotted as magenta squares for AGN models (Feltre et al. 2016; Mignoli et al. 2019) and cyan stars for SFG models (Gutkin et al. 2016). Observed data of UDS-24561 are shown by red circles in both diagnostic diagrams. From the literature, we overlay the data of AGN composite spectra (Hainline et al. 2011; Alexandroff et al. 2013; Le Fèvre et al. 2019; red solid symbols) and SFGs (Stark et al. 2014; Berg et al. 2016, 2018, 2019; Vanzella et al. 2016, 2017, 2020; Amorín et al. 2017; Mainali et al. 2017; Senchyna et al. 2017, 2019; T21a; blue open symbols) at $z = 0 - 7$ in both diagrams. Compared to SFGs, AGN are characterised by smaller O III]/He II and O III]/C IV ratios owing to the hard ionising spectra that power strong He II and C IV emission and triply ionise oxygen.

adopted in Model I in Naidu et al. (2020). Indeed, there is room to relax the adopted escape fraction for non-AGN sources to lower values, depending on the adopted luminosity limit for hosting AGN.

Although our adopted AGN fraction of 20 per cent in luminous $z \simeq 6 - 7$ is arbitrary, we note that Endsley et al. (2021a) find 20 per cent of $z \simeq 7$ sources have intense [O III]+Hβ with EW > 1200 Å and blue UV continua. Furthermore, although we have adopted a constant ionising photon production efficiency (i.e., hydrogen ionising photon production rate per non-ionising UV luminosity at rest-frame 1500 Å) for all sources regardless of luminosity, a higher value for AGN would increase their contribution to the ionising photon budget. These findings illustrate the importance of further examining lower redshift analogues such as UDS-24561.

Given its rarity in the parent sample of extreme [O III] emitters we matched with Chandra data, it may be challenging to find further intermediate redshift AGN similar to UDS-24561. On the other hand, it may be fruitful to focus on extreme [O III] emitters with slightly lower EWs and redder UV slopes given the continuity in the population and the contrast with nearby AGN in Figure 1. By expanding such searches to encompass other wide-field surveys, we can hopefully provide the necessary baseline of properties of low redshift AGN for comparison with targets in the reionisation era.

Ultimately the statistical baseline of spectroscopic properties of blue, extreme [O III] galaxies harbouring AGN at intermediate redshift including UDS-24561 will provide useful clues in guiding future *JWST* emission line surveys in the reionisation era. Since rest-frame UV and optical spectra of $z > 6$ galaxies will be obtained by *JWST*/NIRSpec, AGN activities in these systems could be revealed via broad optical emission features or UV line diagnostics involving high ionisation emission lines like C IV and He II as discussed in Section 3. This will provide a valuable census of AGN at $z > 6$, hence constraining the contribution of AGN to cosmic reionisation.

DATA AVAILABILITY

The 3D-HST data can be accessed from https://archive.stsci. edu/prepds/3d-hst/. The data underlying this article will be shared on reasonable request to the corresponding author.

REFERENCES

Alexandroff R., et al., 2013, MNRAS, 435, 3306
Allen M. G., Groves B. A., Dopita M. A., Sutherland R. S., Kewley L. J., 2008, ApJS, 178, 20
Amorín R., et al., 2017, Nature Astronomy, 1, 0052
Assef R. J., et al., 2010, ApJ, 713, 970
Astropy Collaboration et al., 2013, A&A, 558, A33
Azadi M., et al., 2017, ApJ, 835, 27
Barro G., et al., 2019, ApJS, 243, 22
Berg D. A., Skillman E. D., Henry R. B. C., Erb D. K., Carigi L., 2016, ApJ, 827, 126
Berg D. A., Erb D. K., Auger M. W., Pettini M., Brammer G. B., 2018, ApJ, 859, 164
Berg D. A., Erb D. K., Henry R. B. C., Skillman E. D., McQuinn K. B. W., 2019, ApJ, 874, 93
Bouwens R. J., et al., 2012, ApJ, 754, 83
Bouwens R. J., et al., 2014, ApJ, 793, 115
Bouwens R. J., et al., 2015a, ApJ, 803, 34
Bouwens R. J., Illingworth G. D., Oesch P. A., Caruana J., Holwerda B., Smit R., Wilkins S., 2015b, ApJ, 811, 140
Brammer G. B., et al., 2012, ApJS, 200, 13
Brightman M., Nandra K., Salvato M., Hsu L.-T., Aird J., Rangel C., 2014, MNRAS, 443, 1999
Bruzual G., Charlot S., 2003, MNRAS, 344, 1000
Buchner J., et al., 2015, ApJ, 802, 89
Calzetti D., Kinney A. L., Storchi-Bergmann T., 1994, ApJ, 429, 582
Chevallard J., Charlot S., 2016, MNRAS, 462, 1415
Chevallard J., et al., 2018, MNRAS, 479, 3264
Civano F., et al., 2016, ApJ, 819, 62
Coil A. L., et al., 2015, ApJ, 801, 35
Cristiani S., Serrano L. M., Fontanot F., Vanzella E., Monaco P., 2016, MN-RAS, 462, 2478
Dayal P., Ferrara A., 2018, Phys. Rep., 780, 1
De Barros S., Oesch P. A., Labbé I., Stefanon M., González V., Smit R., Bouwens R. J., Illingworth G. D., 2019, MNRAS, 489, 2355
Du X., Shapley A. E., Tang M., Stark D. P., Martin C. L., Mobasher B., Topping M. W., Chevallard J., 2020, ApJ, 890, 65
Endsley R., Stark D. P., Chevallard J., Charlot S., 2021a, MNRAS, 500, 5229
Endsley R., Stark D. P., Charlot S., Chevallard J., Robertson B., Bouwens R. J., Stefanon M., 2021b, MNRAS, 502, 6044
Erb D. K., Pettini M., Shapley A. E., Steidel C. C., Law D. R., Reddy N. A., 2010, ApJ, 719, 1168
Erb D. K., et al., 2014, ApJ, 795, 33
Fabricant D., et al., 2019, PASP, 131, 075004
Fan X., et al., 2006, AJ, 132, 117
Feltre A., Charlot S., Gutkin J., 2016, MNRAS, 456, 3354
Ferland G. J., et al., 2013, Rev. Mex. Astron. Astrofis., 49, 137
Finkelstein S. L., et al., 2012, ApJ, 756, 164
Finkelstein S. L., et al., 2015, ApJ, 810, 71
Fletcher T. J., Tang M., Robertson B. E., Nakajima K., Ellis R. S., Stark D. P., Inoue A., 2019, ApJ, 878, 87
Förster Schreiber N. M., et al., 2014, ApJ, 787, 38
Freeman W. R., et al., 2019, ApJ, 873, 102
Genzel R., et al., 2014, ApJ, 796, 7
Grazian A., et al., 2018, A&A, 613, A44
Grazian A., et al., 2020, ApJ, 897, 94
Grogin N. A., et al., 2011, ApJS, 197, 35
Gutkin J., Charlot S., Bruzual G., 2016, MNRAS, 462, 1757
Hainline K. N., Shapley A. E., Greene J. E., Steidel C. C., 2011, ApJ, 733, 31
Hainline K. N., Shapley A. E., Greene J. E., Steidel C. C., Reddy N. A., Erb D. K., 2012, ApJ, 760, 74
Hashimoto T., et al., 2015, ApJ, 812, 157
Henry A., Scarlata C., Martin C. L., Erb D., 2015, ApJ, 809, 19
Hirschmann M., Charlot S., Feltre A., Naab T., Somerville R. S., Choi E., 2019, MNRAS, 487, 333
Horne K., 1986, PASP, 98, 609
Hu W., et al., 2017, ApJ, 845, L16

Hunter J. D., 2007, Computing in Science and Engineering, 9, 90
Jaskot A. E., Ravindranath S., 2016, ApJ, 833, 136
Jones E., Oliphant T., Peterson P., et al., 2001, SciPy: Open source scientific tools for Python, http://www.scipy.org/
Kansky J., et al., 2019, PASP, 131, 075005
Kauffmann G., et al., 2003, MNRAS, 346, 1055
Kewley L. J., Maier C., Yabe K., Ohta K., Akiyama M., Dopita M. A., Yuan T., 2013, ApJ, 774, L10
Kocevski D. D., et al., 2018, ApJS, 236, 48
Koekemoer A. M., et al., 2011, ApJS, 197, 36
Kriek M., et al., 2015, ApJS, 218, 15
Labbé I., et al., 2013, ApJ, 777, L19
Laird E. S., et al., 2009, ApJS, 180, 102
Laporte N., Nakajima K., Ellis R. S., Zitrin A., Stark D. P., Mainali R., Roberts-Borsani G. W., 2017, ApJ, 851, 40
Le Fèvre O., et al., 2019, A&A, 625, A51
Leung G. C. K., et al., 2017, ApJ, 849, 48
Leung G. C. K., et al., 2019, ApJ, 886, 11
Loeb A., Barkana R., 2001, ARA&A, 39, 19
Mainali R., Kollmeier J. A., Stark D. P., Simcoe R. A., Walth G., Newman A. B., Miller D. R., 2017, ApJ, 836, L14
Mainali R., et al., 2018, MNRAS, 479, 1180
Marchesi S., et al., 2016, ApJ, 817, 34
Martin C. L., Dijkstra M., Henry A., Soto K. T., Danforth C. W., Wong J., 2015, ApJ, 803, 6
Matthee J., et al., 2021, MNRAS, 505, 1382
McGreer I. D., Mesinger A., D'Odorico V., 2015, MNRAS, 447, 499
McLean I. S., et al., 2012, in McLean I. S., Ramsay S. K., Takami H., eds, Society of Photo-Optical Instrumentation Engineers (SPIE) Conference Series Vol. 8446, Ground-based and Airborne Instrumentation for Astronomy IV. p. 84460J, doi:10.1117/12.924794
Mignoli M., et al., 2019, A&A, 626, A9
Momcheva I. G., et al., 2016, ApJS, 225, 27
Naidu R. P., Tacchella S., Mason C. A., Bose S., Oesch P. A., Conroy C., 2020, ApJ, 892, 109
Nakajima K., et al., 2018, A&A, 612, A94
Nandra K., et al., 2015, ApJS, 220, 10
Oesch P. A., Bouwens R. J., Illingworth G. D., Labbé I., Stefanon M., 2018, ApJ, 855, 105
Oke J. B., Gunn J. E., 1983, ApJ, 266, 713
Onoue M., et al., 2021, arXiv e-prints, p. arXiv:2106.13807
Ouchi M., Ono Y., Shibuya T., 2020, ARA&A, 58, 617
Parsa S., Dunlop J. S., McLure R. J., Mortlock A., 2016, MNRAS, 456, 3194
Planck Collaboration et al., 2020, A&A, 641, A6
Plat A., Charlot S., Bruzual G., Feltre A., Vidal-García A., Morisset C., Chevallard J., Todt H., 2019, MNRAS, 490, 978
Robertson B. E., Ellis R. S., Furlanetto S. R., Dunlop J. S., 2015, ApJ, 802, L19
Saxena A., et al., 2020, A&A, 636, A47
Senchyna P., et al., 2017, MNRAS, 472, 2608
Senchyna P., Stark D. P., Chevallard J., Charlot S., Jones T., Vidal-García A., 2019, MNRAS, 488, 3492
Skelton R. E., et al., 2014, ApJS, 214, 24
Smit R., et al., 2014, ApJ, 784, 58
Smit R., et al., 2015, ApJ, 801, 122
Sobral D., Santos S., Matthee J., Paulino-Afonso A., Ribeiro B., Calhau J., Khostovan A. A., 2018a, MNRAS, 476, 4725
Sobral D., et al., 2018b, MNRAS, 477, 2817
Sobral D., et al., 2019, MNRAS, 482, 2422
Stanway E. R., Eldridge J. J., Becker G. D., 2016, MNRAS, 456, 485
Stark D. P., 2016, ARA&A, 54, 761
Stark D. P., et al., 2014, MNRAS, 445, 3200
Stark D. P., et al., 2015, MNRAS, 454, 1393
Steidel C. C., et al., 2014, ApJ, 795, 165
Tang M., Stark D. P., Chevallard J., Charlot S., 2019, MNRAS, 489, 2572
Tang M., Stark D. P., Chevallard J., Charlot S., Endsley R., Congiu E., 2021a, MNRAS, 501, 3238

Tang M., Stark D. P., Chevallard J., Charlot S., Endsley R., Congiu E., 2021b, MNRAS, 503, 4105

Tilvi V., et al., 2016, ApJ, 827, L14

Vanzella E., et al., 2016, ApJ, 821, L27

Vanzella E., et al., 2017, ApJ, 842, 47

Vanzella E., et al., 2020, MNRAS, 491, 1093

Veilleux S., Cecil G., Bland-Hawthorn J., 2005, ARA&A, 43, 769

Vito F., et al., 2018, MNRAS, 473, 2378

Volonteri M., Reines A. E., Atek H., Stark D. P., Trebitsch M., 2017, ApJ, 849, 155

Xue Y. Q., et al., 2011, ApJS, 195, 10

Xue Y. Q., Luo B., Brandt W. N., Alexander D. M., Bauer F. E., Lehmer B. D., Yang G., 2016, ApJS, 224, 15

This paper has been typeset from a TEX/LATEX file prepared by the author.